International Journal of Heat and Mass Transfer 52 (2009) 1709–1724

Contents lists available at ScienceDirect

International Journal of Heat and Mass Transfer

journal homepage: www.elsevier.com/locate/ijhmt

Three-dimensional modeling of arc plasma and metal transfer in gas metal arc welding

G. Xu [a], J. Hu [b,*], H.L. Tsai [a]

[a] Department of Mechanical and Aerospace Engineering, Missouri University of Science and Technology (formerly University of Missouri-Rolla), 1870 Miner Circle, Rolla, MO 65409, USA
[b] Department of Mechanical Engineering, University of Bridgeport, Bridgeport, CT 06604, USA

ARTICLE INFO

Article history:
Received 12 May 2008
Received in revised form 25 September 2008
Available online 29 November 2008

ABSTRACT

An integrated comprehensive 3D model has been developed to study the transport phenomena in gas metal arc welding (GMAW). This includes the arc plasma, droplet generation, transfer and impingement onto the weld pool, and weld pool dynamics. The continuum formulation is used for the conservation equations of mass, momentum, and energy in the metal zone. The free surface is tracked using the volume-of-fluid (VOF) technique. The 3D plasma arc model is solved for the electric and magnetic fields in the entire domain. The interaction and coupling between the metal zone and the plasma zone is considered. The distributions of velocity, pressure, temperature, and free surface for the metal zone and the velocity, pressure, and temperature for the plasma zone are all calculated as a function of time. The numerical results show the time-dependant distributions of arc pressure, current density, and heat transfer at the workpiece surface are different from presumed Gaussian distributions in previous models. It is also observed that these distributions for a moving arc are non-axisymmetric and the peaks shift to the arc moving direction.

1. Introduction

Gas metal arc welding (GMAW), also referred to by metal inert gas (MIG) welding or metal active gas (MAG) welding, is a welding process in which an electric arc is struck between a consumable electrode and a workpiece. The arc carries electric current and generates intense heat. It ionizes the shielding gas, which consists of inert or active gas, or gas mixture, to its plasma phase. The high temperature plasma melts the filler-metal electrode and periodically generates droplets. A weld pool on the workpiece forms under the influence of both the plasma flow and the droplet impingement. Since the mass transfer and heat transfer in the GMAW process are considerably complicated, most researches and developments in industries are based on the trial and error approach. Even in the experimental studies it is difficult to measure some parameters and determine the detailed weld pool dynamics and droplet formation. Mathematical models have been developed to describe one or two separate components of the process [1–4] or the complete process [5–11]. These models provided a tool to understand the physics behind the complicated GMAW process.

The metal transfer mode in GMAW can be classified to two categories: free-flight transfer and bridging (short-circuiting) transfer [12]. The electric current in the short-circuiting GMAW is low and hence the heat input is low, which makes it suitable for welding thin sheets. A mathematical model for this short-circuiting metal transfer process was developed by Xu et al. [13] to study the effects of some welding parameters, such as welding current and Marangoni force.

The free-flight metal transfer in GMAW can be subdivided into two transfer modes: globular mode with big round droplets repelled from electrode tip and spray mode with small streaming droplets projected from a tapered and rotating electrode tip [12]. The most important parameters affecting the transfer mode and the consequent weld pool include welding current, arc length, shielding gas composition, alloying elements, wire feed speed, diameter of the wire, etc. In order to investigate the effects of some of these parameters, many mathematical models were developed. They were either for a separate component such as droplet (electrode) [4–6], plasma arc [1,5], or weld pool (workpiece) [2–4]; or for a completely integrated system [7–11]. According to a survey article [14], the former is classified as the first-generation arc welding models. Among these separate components the plasma arc is most important since it carries electric current and welding energy. A plasma arc model originally developed for GTAW was modified by Dunn and Eagar [1] to investigate arcs consisting of different shielding gas compositions in GMAW. Because Dunn and Eagar's GMAW arc model simply neglected the influence of metal droplets, it was still similar to GTAW arc models. The significance of the plasma arc model is that once the plasma flow is solved, the arc pressure, current density, and heat flux at the anode and cathode boundaries can be calculated. These boundary values

* Corresponding author. Fax: +1 203 576 4765.
E-mail address: jjhu@bridgeport.edu (J. Hu).

0017-9310/$ - see front matter © 2008 Elsevier Ltd. All rights reserved.
doi:10.1016/j.ijheatmasstransfer.2008.09.018

Nomenclature

A_v	constant, defined in Eq. (35)
$\vec{B}$	magnetic field vector
B_x, B_y, B_z	magnetic field in x, y, and z direction
B_θ	azimuthal magnetic field
C	specific heat, or color function
c_1, c_2	color functions in fluid 1 and 2
C	coefficient, defined in Eq. (15)
C_{ds}	drag coefficient
C_1	permeability coefficient, defined in Eq. (14)
d	dendrite arm spacing
D_d	droplet diameter
e	elementary charge
F	volume-of-fluid function
F_{drag}	plasma drag force
$\vec{F}_{sv}$	surface tension volume force
$\vec{F}_{pa}$	plasma arc pressure volume force
f	mass fraction
g	volume fraction or gravitational acceleration
h	enthalpy
H	latent heat of fusion
H_{ev}	latent hat of vaporization
I	welding current
$\vec{j}$	current density vector
j_a	current density at anode
j_x, j_y, j_z	current density at x, y, and z direction
k	thermal conductivity
K	permeability, defined in Eq. (13)
kb	Boltzmann constant
k_{eff}	effective thermal conductivity
$\vec{n}$	normal vector to the free surface
p	pressure
p_s	surface tension pressure
P_{atm}	atmosphere pressure
q_{ev}	evaporation mass rate of metal vapor
r	radial distance from the electrode axis
R_a	radius of the electrode
R_e	Reynolds number
$\vec{s}$	tangential vector to the free surface
S_a	anode energy source term for the metal
S_{ap}	anode energy source term for the plasma arc
S_c	cathode energy source term for the metal
S_{cp}	cathode energy source term for the plasma arc
$\vec{S}_m$	momentum source term for the metal
S_R	radiation heat loss
t	time
T	temperature
$T_{p,a}$,$T_{p,c}$	arc plasma temperature adjacent to the anode and cathode
T_a,T_c	temperature of anode and cathode
T_l	liquidus temperature
T_s	solidus temperature
u, v, w	velocity in x, y, and z direction
$\vec{V}$	velocity vector
$\vec{V}_r$	relative velocity vector
V_c	cathode fall voltage
w_g	axial plasma velocity
x, y, z	Cartesian coordinate system

Greek symbols

γ	surface tension coefficient
ε	radiation emissivity
κ	free surface curvature
μ_l	dynamic viscosity
μ_g	dynamic viscosity of plasma
ϕ	electric potential
ϕ_w	work function of the anode material
σ_e	electrical conductivity
ρ	density
ρ_g	density of plasma
τ_{ij}	stress tensor
$\vec{\tau}_{Ms}$	Marangoni shear stress
$\vec{\tau}_{ps}$	plasma shear stress
δ	effective heat transfer length

Subscripts

a	anode
c	cathode
l	liquid phase
s	solid phase

Superscripts

n	time step n
$n+1$	time step $n+1$

are necessary for weld pool and droplet models. However, most researchers used the presumed distributions of these boundary values in their models in order to significantly cut the computational efforts and achieve relatively reasonable numerical results at the same time. The Gaussian distributions with carefully selected mean and variance values were normally assumed. For example, Hu et al. [3] utilized such assumptions in their droplet-impinged weld pool model. Other non-Gaussian distribution formulas were also utilized based on experimental results. Particularly, Wang et al. [4] used the integral formulas for the distributions of current density and heat flux in their droplet generations model.

Though the separated models for each component were generally able to obtain good numerical results, their presumed boundary conditions are arbitrary and can be inaccurate. A more rigorous model needs to integrate all the components. This kind of model is classified as the second-generation arc welding model [14] and its development is one of the research objectives of many researchers. Fan and Kovacevic [11] have developed such a unified 2D model for the globular metal transfer in GMAW. Hu and Tsai [7–10] developed a completely integrated 2D model and studied metal transfer and arc plasma characteristics. Haidar's earlier unified model [6] focused on the metal droplet formation and the predicted droplet diameter, droplet detachment frequency, and transition from globular to spray transfer mode and the results agreed with experimental measurements.

All the aforementioned complete models are two-dimensional, thus applicable only to the stationary axisymmetric arc welding. In a real world welding, the arc is moving, the weld pool is non-axisymmetric, and the heat flux and current density at the workpiece are greatly affected by the weld pool shape [15]. In addition, the geometries of many weld joints such as T joint, lap joint, corner joint, and groove weld butt joint are naturally three-dimensional. Finally, perturbations such as external magnetic field may deflect axisymmetric plasma arc from its axisymmetry [16]. A 3D model is necessary to investigate all these applications. Most previous 3D attempts focused on the weld pool, but almost all of them still used the axisymmetric assumptions for boundary conditions [2,3].

In order to calculate the true 3D boundary values such as arc pressure, heat flux, and current density, a non-axisymmetric plasma arc model is a prerequisite. Though mathematical models of axisymmetric arc were well formulated, very little research work has been done on non-axisymmetric arc. The major difficulty for this extension is the calculation of the self-induced magnetic field, which is not azimuthal and cannot be simply calculated using the integration from Ampere's law as in the 2D models. Recently, Xu and Tsai [17] developed a 3D plasma arc model, in which the magnetic field and electric current vectors were solved using derived Maxwell's equations. Their model paved the way toward the development of a complete 3D arc welding model.

In this article, a 3D mathematical model for the plasma arc and metal transfer in GMAW is presented. This model is sufficient to describe the complete 3D GMAW process, but the transient solution of this complete model is extremely time-consuming and is beyond the capability of current PCs. Therefore, simplifications were made at the interface of the metal and plasma arc to reduce the transient coupling of the plasma arc and metal. In order to study the plasma arc interaction with metal during the metal transfer process, the presented results were based on a simplified approach of droplet generation and its transfer in the plasma arc. The properties of the plasma arc during the droplet transfer process were investigated.

2. Mathematical model

2.1. Governing equations

Fig. 1 shows a schematic sketch of a GMAW process. In the common direct current electrode positive (DCEP) connection, the electrode is the anode and the workpiece is the cathode. A plasma arc is struck between the electrode and the workpiece. The electrode is continuously fed downward and melts at the tip by the high temperature arc. Droplets are then detached from the electrode and transferred to the workpiece. The computational domain includes an anode zone (electrode), an arc zone, and a cathode zone (workpiece). The anode and cathode sheaths have been omitted and treated as special boundary conditions for computational simplifications. Assuming the arc is in local thermal equilibrium (LTE) and the plasma flow is laminar and incompressible, the differential equations governing the arc, the electrode, detached droplet, and the workpiece can be put into a single set.

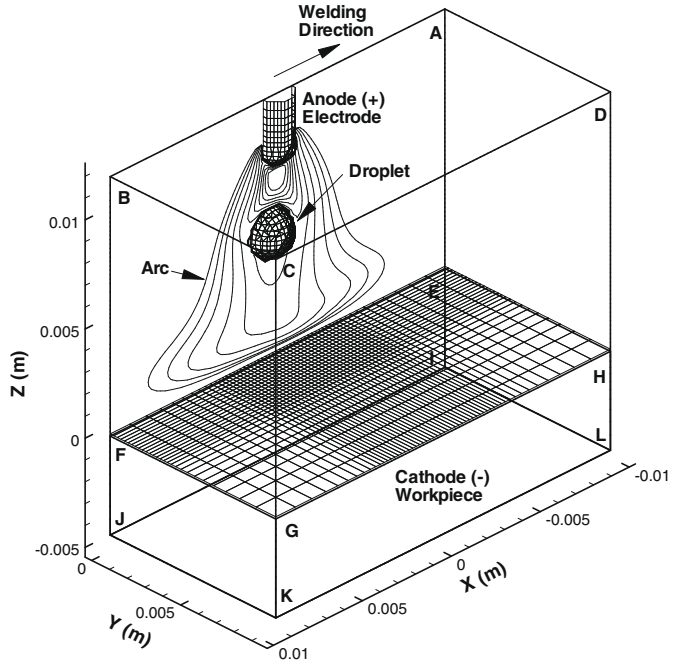

Fig. 1. A schematic representation of a GMAW process.

The differential equations governing the conservations of mass, momentum, and energy based on continuum formulation given by Chiang and Tsai [18] are modified and employed in this study. The derivation of the equations can be found in [19]. The idea of continuum formulation is to eliminate the need of explicitly tracking the solidifying or melting interface, and therefore the established conversation equations is valid for both solid and liquid phases. The internal mushy zone in this formulation is modeled using semi-empirical laws of transport behavior with principles of classical mixture theory. These differential equations are given below:

Mass continuity

$$\frac{\partial \rho}{\partial t} + \nabla \cdot (\rho \vec{V}) = 0 \tag{1}$$

X-momentum

$$\frac{\partial(\rho u)}{\partial t} + \nabla \cdot (\rho \vec{V} u) = -\frac{\partial p}{\partial x} + \nabla \cdot \left(\mu_l \frac{\rho}{\rho_l \nabla u}\right) - \frac{\mu_l}{K}\frac{\rho}{\rho_l}(u - u_s) - \frac{C\rho^2}{K^{1/2}\rho_l}|u - u_s|(u - u_s) - \nabla \cdot (\rho f_s f_l \vec{V}_r u_r) + j_y B_z - j_z B_y \tag{2}$$

Y-momentum

$$\frac{\partial(\rho v)}{\partial t} + \nabla \cdot (\rho \vec{V} v) = -\frac{\partial p}{\partial y} + \nabla \cdot \left(\mu_l \frac{\rho}{\rho_l \nabla v}\right) - \frac{\mu_l}{K}\frac{\rho}{\rho_l}(v - v_s) - \frac{C\rho^2}{K^{1/2}\rho_l}|v - v_s|(v - v_s) - \nabla \cdot (\rho f_s f_l \vec{V}_r v_r) + j_z B_x - j_x B_z \tag{3}$$

Z-momentum

$$\frac{\partial(\rho w)}{\partial t} + \nabla \cdot \left(\rho \vec{V} w\right) = -\frac{\partial p}{\partial z} + \nabla \cdot (\mu_l \frac{\rho}{\rho_l \nabla w}) - \frac{\mu_l}{K}\frac{\rho}{\rho_l}(w - w_s) - \frac{C\rho^2}{K^{1/2}\rho_l}|w - w_s|(w - w_s) - \nabla \cdot (\rho f_s f_l \vec{V}_r w_r) + \rho g + F_{drag} + j_x B_y - j_y B_x \tag{4}$$

Energy

$$\frac{\partial(\rho h)}{\partial t} + \nabla \cdot (\rho \vec{V} h) = \nabla \cdot \left(\frac{k}{c_s}\nabla h\right) + \nabla \cdot \left(\frac{k}{c_s}\nabla(h_s - h)\right) - \nabla \cdot (\rho(\vec{V} - \vec{V}_s)(h_l - h)) + \frac{j_x^2 + j_y^2 + j_z^2}{\sigma_e} - S_r + \frac{5k_b}{2e}\left(\frac{j_x}{c_p}\frac{\partial h}{\partial x} + \frac{j_y}{c_p}\frac{\partial h}{\partial y} + \frac{j_z}{c_p}\frac{\partial h}{\partial z}\right) \tag{5}$$

In Eqs. (1)–(5), u, v, and w are the velocity components in the x, y and z directions, respectively; $\vec{V}$ is velocity vector; $\vec{V}_r = \vec{V}_l - \vec{V}_s$ is the relative velocity vector between the liquid phase and the solid phase; the subscripts s and l refer to the solid and liquid phases, respectively; p is the pressure; T is the temperature; h is the enthalpy; f is the mass fraction of the liquid or solid; K is the permeability function; C is the inertial coefficient; ρ is the density; μ is the viscosity; k is the thermal conductivity; c is the specific heat; g is the gravitational acceleration; F_{drag} is the plasma drag force; j_x, j_y, and j_z are the current density components in the x, y and z directions, respectively; B_x, B_y, and B_z are the magnetic field components in the x, y and z directions, respectively; σ_e is the electrical conductivity; S_R is the radiation heat loss; k_b is the Stefan-Boltzmann constant; and e is the electronic charge.

The third and fourth terms on the right-hand side of Eqs. (2)–(4) represent the first and second order drag forces of the flow in the mushy zone. The fifth term represents an interaction between the solid and the liquid phases due to the relative velocity. The second term on the right-hand side of Eq. (5) represents the net Fourier diffusion flux. The third term represents the energy flux associated with the relative phase motion. All these aforementioned terms in this paragraph are zero except in the mushy zone. In addition, the solid phase is assumed to be stationary ($\vec{V}_s = 0$).

The plasma drag force F_{drag} is only for the in-flight droplets and its formula is given later. The last three terms in Eq. (5) are Ohmic heating, radiation loss, and energy transfer due to electron flow, respectively. The last two terms in the momentum Eqs. (2)–(4) represent the respective components of the electromagnetic force vector.

The continuum density, velocity, and enthalpy in Eqs. (1)–(5) are defined as

$$\rho = g_s\rho_s + g_l\rho_l \tag{6}$$

$$\vec{V} = f_s\vec{V}_s + f_l\vec{V}_l \tag{7}$$

$$h = f_s h_s + f_l h_l \tag{8}$$

The solid mass fraction and liquid mass fraction are defined as, respectively, as

$$f_s = \frac{g_s\rho_s}{\rho}, \quad f_l = \frac{g_l\rho_l}{\rho} \tag{9}$$

The mixture thermal conductivity is given by

$$k = g_s k_s + g_l k_l \tag{10}$$

If the phase specific heats are assumed to be constant, phase enthalpies in Eq. (8) can be expressed as

$$h_s = c_s T, h_l = c_l T + (c_s - c_l)T_l + H \tag{11}$$

where H is the latent heat; T_l is the liquidus temperature; g_s and g_l are the volume fractions of the solid and liquid phases, respectively. If the latent heat of solidification is assumed to be released linearly between solidus temperature T_s and liquidus temperature T_l, the volume fraction of sold phase can be calculated by

$$g_s = \frac{T_l - T}{T_l - T_s} \tag{12}$$

The flow in the multiphase region (mushy zone) is assumed to be analogous to the flow in porous media. The permeability K in Eqs. (2)–(4) is calculated using the Carman-Kozeny equation [20]

$$K = \frac{g_l^3}{C_1(1-g_l)^2} \tag{13}$$

The value of C_1 depends on the morphology of the porous media. In this study, C_1 is expressed as [21]

$$C_1 = \frac{180}{d^2} \tag{14}$$

where d is proportional to the dendrite dimension, which is assumed to be a constant and is of the order of 10^{-2} cm. The inertial coefficient in Eqs. (2)–(4), C, can be calculated from [22]

$$C = 0.13 g_l^{-3/2} \tag{15}$$

In the pure solid phase ($g_l = 0$) and in pure liquid phase ($g_l = 1$), Eq. (13) is reduced to the appropriate limits $K = 0$ and $K = \infty$, respectively. In this continuum model, the solid-liquid phase boundary is embedded in the continuum solution and does not need to be explicitly tracked. The momentum Eqs. (2)–(4) become trivial for the solid phase because $\vec{V} = \vec{V}_s = 0$. For the liquid and gas phases, the ordinary Navier-Stokes equations will be recovered because the permeability K is infinity and solid mass fraction f_s is zero.

2.2. Electrical potential and magnetic field

The current density components j_x, j_y, and j_z required in Eqs. (2)–(5) are obtained by solving for the electric potential ϕ from the following current continuity equation

$$\nabla\cdot(\sigma_e\nabla\phi) = \frac{\partial}{\partial x}\left(\sigma_e\frac{\partial\phi}{\partial x}\right) + \frac{\partial}{\partial y}\left(\sigma_e\frac{\partial\phi}{\partial y}\right) + \frac{\partial}{\partial z}\left(\sigma_e\frac{\partial\phi}{\partial z}\right) = 0 \tag{16}$$

and using Ohm's law

$$j_x = -\sigma_e\frac{\partial\phi}{\partial x}, \quad j_y = -\sigma_e\frac{\partial\phi}{\partial y}, \quad j_z = -\sigma_e\frac{\partial\phi}{\partial z} \tag{17}$$

The magnetic field components B_x, B_y, and B_z are required to calculate the electromagnetic forces for momentum Eqs. (2)–(4). The equations needed to calculate the magnetic field can be derived from Ampere's law $\nabla\times\vec{B} = \mu_0\vec{j}$ [5]. By taking the cross product on both sides and applying the following vector identity

$$\nabla\times(\nabla\times\vec{B}) = -\nabla^2\vec{B} + \nabla(\nabla\cdot\vec{B}) = -\nabla^2\vec{B} \tag{18}$$

where $\nabla\cdot\vec{B} = 0$ is basically the Gauss's law for magnetism, which means the absence of magnetic monopoles. The Ampere's law can be rewritten in the following conservation form [23]

$$\nabla^2\vec{B} = -\mu_0(\nabla\times\vec{j}) \tag{19}$$

Eq. (19) is the Poisson vector equation and has the following three components

$$\frac{\partial^2 B_x}{\partial x^2} + \frac{\partial^2 B_x}{\partial y^2} + \frac{\partial^2 B_x}{\partial z^2} = -\mu_0\left(\frac{\partial j_z}{\partial y} - \frac{\partial j_y}{\partial z}\right) \tag{20}$$

$$\frac{\partial^2 B_y}{\partial x^2} + \frac{\partial^2 B_y}{\partial y^2} + \frac{\partial^2}{\partial z^2} = -\mu_0\left(\frac{\partial j_x}{\partial z} - \frac{\partial j_z}{\partial x}\right) \tag{21}$$

$$\frac{\partial^2 B_z}{\partial x^2} + \frac{\partial^2 B_z}{\partial y^2} + \frac{\partial^2 B_z}{\partial z^2} = -\mu_0\left(\frac{\partial j_y}{\partial x} - \frac{\partial j_x}{\partial y}\right) \tag{22}$$

2.3. Free surface and surface tension

The volume-of-fluid (VOF) technique [24] is used to track the free surface of the droplet and weld pool. In this technique, a volume-of-fluid function, $F(x, y, z, t)$, is defined to indicate the topology of metal flow. This function represents the volume of fluid per unit volume and satisfies the following equation

$$\frac{dF}{dt} = \frac{\partial F}{\partial t} + (\vec{V}\cdot\nabla)F = 0 \tag{23}$$

According to the definition, a unit value of F corresponds to cells full of fluid (metal), while a zero value corresponds to cells empty of fluid. Cells with F values between zero and one are partially filled with fluid and indicate the free surface cells.

Fluid surface is subject to surface tension because the molecular forces at the surface change abruptly as the fluid properties change discontinuously. The surface tension pressure normal to the free surface can be expressed as [25]

$$p_s = \gamma\kappa \tag{24}$$

where γ is the surface tension coefficient and κ is the free surface curvature. The continuum surface force (CSF) model proposed in [25] is employed to interpret surface forces as continuous volume forces across the interface. The surface tension volume force is given by [25]

$$\vec{F}_{sv} = \gamma\kappa\frac{\nabla\tilde{c}}{[c]} \tag{25}$$

where $[c]$ is the jump in color and $\tilde{c}$ is the mollified color function that varies smoothly over a transition region across the interface.

Because $\nabla\tilde{c}$ is nonzero only the in the transition region, the surface volume force also is nonzero only in the transition region. The local curvature in Eq. (24) is calculated by

$$\kappa = -\left[\nabla\cdot\left(\frac{\vec{n}}{|\vec{n}|}\right)\right] = \frac{1}{|\vec{n}|}\left[\left(\frac{\vec{n}}{|\vec{n}|}\cdot\nabla\right)|\vec{n}| - (\nabla\cdot\vec{n})\right] \tag{26}$$

where $\vec{n}$ is a vector normal to the local free surface and is given by $\vec{n} = \nabla\tilde{c}$.

The volume-of-fluid F function is chosen as the color function for the above calculations in this study. The simplified quadratic-like interpolation was adopted for the mollified color function. The 3D extension of the classic CSF surface tension model in [25] was implemented.

The temperate-dependent Marangoni shear stress tangential to the local free surface is given by

$$\vec{\tau}_{\mathrm{Ms}} = \frac{\partial\gamma}{\partial T}\frac{\partial T}{\partial\vec{s}} \tag{27}$$

where $\vec{s}$ is the vector tangential to the local free surface. The tangential gradient vector can be calculated from the known local normal vector ($\nabla_s T = \nabla T - \nabla_N T$).

2.4. Internal boundary conditions at the plasma arc and metal interface

In this study, the computational domain is divided into arc domain (arc column and shielding gas) and metal domain (electrode, detached droplet, and workpiece). The current distribution is determined by the thermophysical properties of the two domains, thus the current continuity and magnetic field equations are solved in the entire computational domain. Other primary variables, including p, u, v, and T, are calculated separately in the metal domain and arc domain. As the velocity of the metal domain is much smaller than the velocity of the arc plasma, the metal region serves as an inner obstacle in the arc domain. In the metal domain, the arc region is considered as void. The two domains are coupled through interfacial boundary conditions. VOF Eq. (23) is solved in the metal domain to track the moving free surface of the electrode, droplet and weld pool with free boundary conditions set at the metal surface.

2.4.1. Internal momentum boundary conditions

Additional body force source terms are added to the momentum equations in metal domain at the metal free surface to consider the effects of surface tension, Marangoni shear stress, arc plasma shear stress and arc pressure. Arc pressure volume force can be added in the same way as that for surface tension by

$$\vec{F}_{\mathrm{pa}} = p_{\mathrm{a}}\frac{\nabla\tilde{c}}{[c]} \tag{28}$$

where p_{a} is the arc pressure at the metal surface.

The plasma shear stress on metal surface is calculated by

$$\vec{\tau}_{\mathrm{ps}} = \mu_{\mathrm{g}}\frac{\partial\vec{V}}{\partial\vec{s}} \tag{29}$$

where μ_{g} is the viscosity of the plasma and $\vec{V}$ is the plasma velocity vector.

The additional momentum source term to account for plasma transient effects on the metal surface is calculated in metal domain by

$$\vec{S}_{\mathrm{m}} = \vec{F}_{\mathrm{sv}} + \vec{\tau}_{\mathrm{Ms}} + \vec{F}_{\mathrm{pa}} + \vec{\tau}_{\mathrm{ps}} \tag{30}$$

However, as the fully transient solutions of plasma flow are too computationally expensive, the effects of the plasma arc on the metal surface are often neglected or represented by empirical formulas. In this study, an empirical plasma drag force formula is used to account for the plasma drag effect on the in-flight droplet in Eq. (4) [26]

$$F_{\mathrm{drag}} = C_{\mathrm{ds}}\frac{1}{2}\rho_{\mathrm{g}}w_{\mathrm{g}}^2\left(\frac{\pi D_{\mathrm{d}}^2}{4}\right) \tag{31}$$

where C_{ds} is the drag coefficient for a sphere; ρ_{g} is the plasma gas density; w_{g} is the assumed plasma gas velocity; and D_{d} is the droplet diameter. The drag coefficient depending on the Reynolds number is given by [26]

$$C_{\mathrm{ds}} = \frac{24}{R_e} + \frac{6}{\sqrt{1+R_e}} + 0.4 \qquad \text{for} \quad 0 < R_e < 200{,}000 \tag{32}$$

where $R_e = \rho_{\mathrm{g}}w_{\mathrm{g}}D_{\mathrm{d}}/\mu_{\mathrm{g}}$. The properties of plasma are evaluated at the temperature of 15,000 K and the velocity of plasma is assumed to be 100 m/s.

Neglecting the plasma arc effect on the droplet and Marangoni shear stress on the metal surface, the internal momentum boundary conditions for the metal domain in the current study are represented by

$$\vec{S}_{\mathrm{m}} = \vec{F}_{\mathrm{sv}} + \vec{F}_{\mathrm{drag}} \tag{33}$$

2.4.2. Internal energy boundary conditions

At the internal plasma-metal interfaces, there exist an anode sheath and a cathode sheath, which are thin boundary regions near the anode and the cathode. In the anode and cathode sheaths, the mixture of plasma and metal vapor departs from the Local Thermodynamics Equilibrium (LTE). Therefore, the energy balance across this region can not be accurately calculated through a simple one-temperature model [27,28]. In order to eliminate the complexity, a straightforward source term, S_{a}, is used to account for the heat transfer from the plasma arc to the anode [7]

$$S_{\mathrm{a}} = k_{\mathrm{eff}}\frac{T_{\mathrm{p,a}} - T_{\mathrm{a}}}{\delta} + J_{\mathrm{a}}\phi_{\mathrm{w}} - \varepsilon k_{\mathrm{b}}T_{\mathrm{a}}^4 - q_{\mathrm{ev}}H_{\mathrm{ev}} \tag{34}$$

where k_{eff} represents the effective thermal conductivity and δ is the thickness of the anode region. These two parameters can be adjusted to fit the experimental results. $T_{\mathrm{p,a}}$ is the plasma temperature adjacent to the anode; T_{a} is the anode temperature; J_{a} is the anode

Table 1
External boundary conditions for the momentum and energy equations in the plasma arc domain.

	BCKJ	ADLI	CDLK	BAIJ	ABCD	IJKL
u	$\frac{\partial(\rho u)}{\partial x} = 0$	$\frac{\partial(\rho u)}{\partial x} = 0$	$\frac{\partial u}{\partial y} = 0$	$\frac{\partial u}{\partial y} = 0$	0	–[a]
v	$\frac{\partial v}{\partial x} = 0$	$\frac{\partial v}{\partial x} = 0$	$\frac{\partial(\rho v)}{\partial y} = 0$	0	0	–[a]
w	$\frac{\partial w}{\partial x} = 0$	$\frac{\partial w}{\partial x} = 0$	$\frac{\partial w}{\partial y} = 0$	$\frac{\partial w}{\partial y} = 0$	$\frac{\partial(\rho w)}{\partial z} = 0$	–[a]
	T = 300K (inflow)	T = 300K (inflow)	T = 300K (inflow)		T = 300K (inflow)	
h	$\frac{\partial T}{\partial x} = 0$ (outflow)	$\frac{\partial T}{\partial x} = 0$ (outflow)	$\frac{\partial T}{\partial y} = 0$ (outflow)	$\frac{\partial T}{\partial y} = 0$	$\frac{\partial T}{\partial z} = 0$ (outflow)	–[a]

[a] Momentum and energy equations not solved in the solid domain.

Table 2
External boundary conditions for the electric potential and magnetic field equations in the plasma arc domain.

	BCKJ	ADLI	CDLK	BAIJ	ABCD	IJKL
ϕ	$\frac{\partial\phi}{\partial x}=0$	$\frac{\partial\phi}{\partial x}=0$	$\frac{\partial\phi}{\partial y}=0$	$\frac{\partial\phi}{\partial y}=0$	$-\sigma_e\frac{\partial\phi}{\partial z}=\frac{I}{\pi}R_a^2$, $r<R_a$[a]; $\frac{\partial\phi}{\partial z}=0, r>R_a$[a]	0
B_x	$\frac{\partial B_x}{\partial x}=0$	$\frac{\partial B_x}{\partial x}=0$	$\frac{\partial B_x}{\partial y}=0$	0	$\frac{y}{r}\left(\frac{\mu_0 I}{2\pi r}\right), r>R_a$[a]; $\frac{y}{r}\left(\frac{r\mu_0 I}{2\pi R_a^2}\right), r<R_a$[a]	$\frac{\partial B_x}{\partial z}=0$
B_y	$\frac{\partial B_y}{\partial x}=0$	$\frac{\partial B_y}{\partial x}=0$	$\frac{\partial B_y}{\partial y}=0$	$\frac{\partial B_y}{\partial y}=0$	$-\frac{x}{r}\left(\frac{\mu_0 I}{2\pi r}\right), r>R_a$[a]; $-\frac{x}{r}\left(\frac{r\mu_0 I}{2\pi R_a^2}\right), r<R_a$[a]	$\frac{\partial B_y}{\partial z}=0$
B_z	$\frac{\partial B_z}{\partial x}=0$	$\frac{\partial B_z}{\partial x}=0$	$\frac{\partial B_z}{\partial y}=0$	$\frac{\partial B_z}{\partial y}=0$	0	$\frac{\partial B_z}{\partial z}=0$

[a] R_a is the radius of the electrode and $r=\sqrt{x^2+y^2}$.

Table 3
External boundary conditions for the momentum and energy equations in metal domain.

	BCKJ	ADLI	CDLK	BAIJ	ABCD	IJKL
u	Welding speed	Welding speed	0	$\frac{\partial u}{\partial y}=0$	0	0
v	0	0	0	0	0	0
w	0	0	0	$\frac{\partial w}{\partial y}=0$	Electrode feed speed	0
T	$\frac{\partial T}{\partial x}=0$	$\frac{\partial T}{\partial x}=0$	$\frac{\partial T}{\partial y}=0$	$\frac{\partial T}{\partial y}=0$	T = 1000 K	$\frac{\partial T}{\partial z}=0$

Table 4
Thermophysical properties of mild steel and other parameters.

Nomenclature	Symbol	Value (unit)
Constant in Eq. (35)	A_v	2.52
Specific heat of solid phase	c_s	700 (J kg^{-1} K^{-1})
Specific heat of liquid phase	c_l	780 (J kg^{-1} K^{-1})
Thermal conductivity of solid phase	k_s	22 (W m^{-1} K^{-1})
Thermal conductivity of liquid phase	k_l	22 (W m^{-1} K^{-1})
Density of solid phase	ρ_s	7200 (kg m^{-3})
Density of liquid phase	ρ_l	7200 (kg m^{-3})
Radiation emissivity	ε	0.4
Dynamic viscosity	μ_l	0.006 (kg m^{-1} s^{-1})
Latent heat of fusion	H	2.47×10^5 (J kg^{-1})
Latent heat of vaporization	H_{ev}	7.34×10^6 (J kg^{-1})
Solidus temperature	T_s	1750 (K)
Liquidus temperature	T_l	1800 (K)
Surface tension coefficient	γ	1.2 (N m^{-1})
Surface tension temperature gradient	$\partial\gamma\partial T$	10^{-4} (N m^{-1} K^{-1})
Electrical conductivity	σ_e	7.7×10^5 (Ω^{-1} m^{-1})
Work function	ϕ_w	4.3 V

current density and may have three components in x, y, and z directions; ϕ_w is the work function of the anode material; ε is the emissivity of the anode; q_{ev} is the mass evaporation rate of anode metal; and H_{ev} is the latent heat of evaporation. For the metal of steel, q_{ev} can be expressed as [29]

$$\log(q_{ev}) = A_v + \log(P_{atm}) - 0.5\log(T_a) \tag{35}$$

$$\log(P_{atm}) = 6.121 - \frac{18836}{T_a} \tag{36}$$

where A_v is material-dependant constant and is listed in Table 4 for steel.

At the arc-anode interface, the energy equation for the plasma only considers the cooling effects through conduction and the source term, S_{ap}, is given as

$$S_{ap} = k_{eff}\frac{T_{p,a}-T_a}{\delta} \tag{37}$$

Similarly, source terms, S_c and S_{cp} are used to represent the heat transfer from plasma arc to cathode rand cathode to plasma arc, respectively [7]

$$S_c = k_{eff}\frac{T_{p,c}-T_c}{\delta} - \varepsilon k_b T_c^4 - q_{ev}H_{ev} \tag{38}$$

$$S_{cp} = k_{eff}\frac{T_{p,c}-T_c}{\delta} \tag{39}$$

where $T_{p,c}$ is the plasma temperature adjacent to the cathode; T_c is the cathode temperature, and δ is the thickness of the cathode region.

Because the computation of the coupled heat transfer between the plasma and metal is extremely expensive, the heat transfer in the electrode is not calculated and the thermal effect of plasma arc on the workpiece is neglected. The temperature of the electrode is assumed to be 1000 K and the detached droplet 3000 K. For the arc domain, the temperatures of the electrode and workpiece are assumed to be 1000 K. The sensitivity study in [1] showed the surface temperature of the electrode and workpiece had insignificant effect on the plasma arc.

2.5. External boundary conditions of the computational domain

2.5.1. Momentum and energy boundary conditions for the arc domain

As the thermal physical properties vary significantly only in the arc domain, the current continuity and magnetic field equations are coupled with the arc domain. Table 1 lists the external boundary conditions of the momentum and energy equations in the arc domain. The top plane ABCD is the inflow anode region. The velocity components in x and y directions are assumed to be zero and the gradient of mass flow in z direction $\partial(\rho w)/\partial z$ is assumed to be zero. The inlet gas temperature is assumed to be 300 K. Sensitivity analyses has shown the inlet temperature has an insignificant effect on the arc column [1]. The gradient of mass flow $\partial(\rho u)/\partial x$ is assumed to be zero for the planes ADHE and BCGF. $\partial(\rho v)/\partial y$ is assumed to be zero for the plane CDHG. The temperature boundary condition representing the inflow is taken as 300 K. This value is arbitrary and the sensitivity studies have shown that the arc column is not affected significantly by this temperature value [1]. This is because the variation of specific heat outside the arc column is very small and does not cause a large change to the energy equation [1]. For the outflow, the gradients of temperature, $\partial T/\partial x$ and $\partial T/\partial y$, are assumed to be zero. The boundary conditions at the symmetric plane BAIJ is straightforward. The velocity component in y direction is zero. The gradients of velocity, $\partial u/\partial y$ and $\partial w/\partial y$, and the gradient of temperature $\partial T/\partial y$ are zero.

2.5.2. Electric potential and magnetic field boundary conditions

The boundary conditions for the electric potential and the magnetic field need to be imposed for the whole domain. The complete listing of electric potential and magnetic field boundary conditions is given in Table 2. The bottom plane of the workpiece IJKL is taken

to be isopotential ($\phi = 0$). The welding current is assumed to be uniformly distributed when it flows into the electrode. The gradient of electric potential for the electrode boundary becomes

$$-\sigma_e \frac{\partial \phi}{\partial z} = \frac{I}{\pi R_a^2}, \quad r < R_a \tag{40}$$

where $r = \sqrt{x^2 + y^2}$ is the distance from the electrode axis; R_a is the radius of the electrode; and I is the welding current. The gradient of electric potential for the top boundary plane ($r > R_a$), the symmetric plane, and all side boundary planes are assumed to be zero.

The magnetic field at the top plane ABCD is assumed to be azimuthal. From Ampere's law, the azimuthal magnetic field B_θ is given as

$$B_\theta = \frac{r\mu_0 I}{2\pi R_a^2}, \quad r < R_a \tag{41}$$

$$B_\theta = \frac{\mu_0 I}{2\pi r}, \quad r > R_a \tag{42}$$

The z component is zero in the azimuthal assumption, thus the projected x and y components are

$$B_x = \frac{y}{r} B_\theta, \quad B_y = -\frac{x}{r} B_\theta \tag{43}$$

For all the side planes and the bottom plane of the workpiece, the gradient of magnetic field is simply assumed to be zero. For the symmetric plane BAIJ, B_x is zero and the gradients of magnetic field $\partial B_y/\partial y$ and $\partial B_z/\partial y$ are zero.

2.5.3. Momentum and energy boundary conditions for the metal domain

Table 3 shows the complete list of the external momentum and energy boundary conditions. The electrode moves downward at the wire feed speed and the workpiece moves relatively to the electrode at the welding speed. The workpiece is considered as insulated at the sides and bottom.

3. Numerical considerations

For the metal domain, the method developed by Torrey et al. [24,30] was used to solve p, u, v, and T. This method is Eulerian and allows for an arbitrary number of segments of free surface

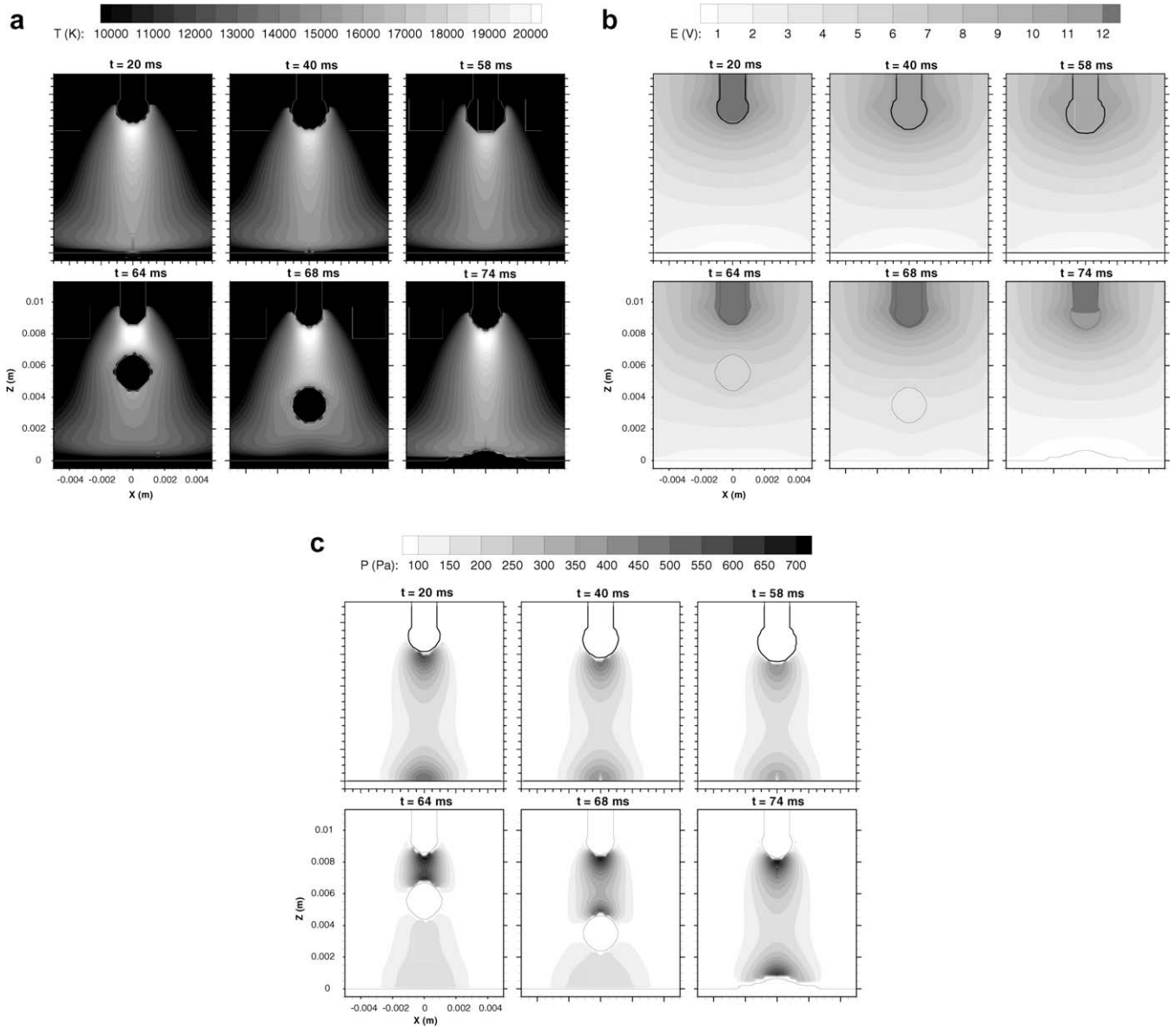

Fig. 2. A typical sequences of temperature, electrical potential, and pressure distributions on the symmetric plane ($y = 0$) for an axisymmetric stationary arc: (a) temperature, (b) electrical potential, (c) pressure.

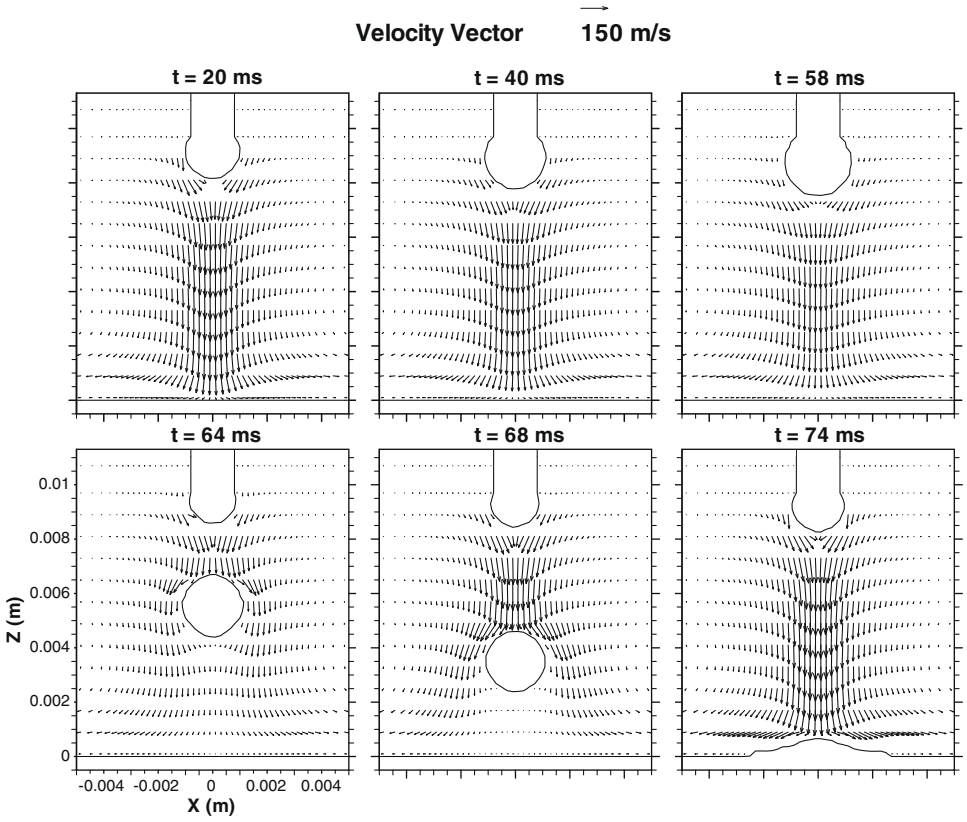

Fig. 3. The corresponding velocity distributions as shown in Fig. 2.

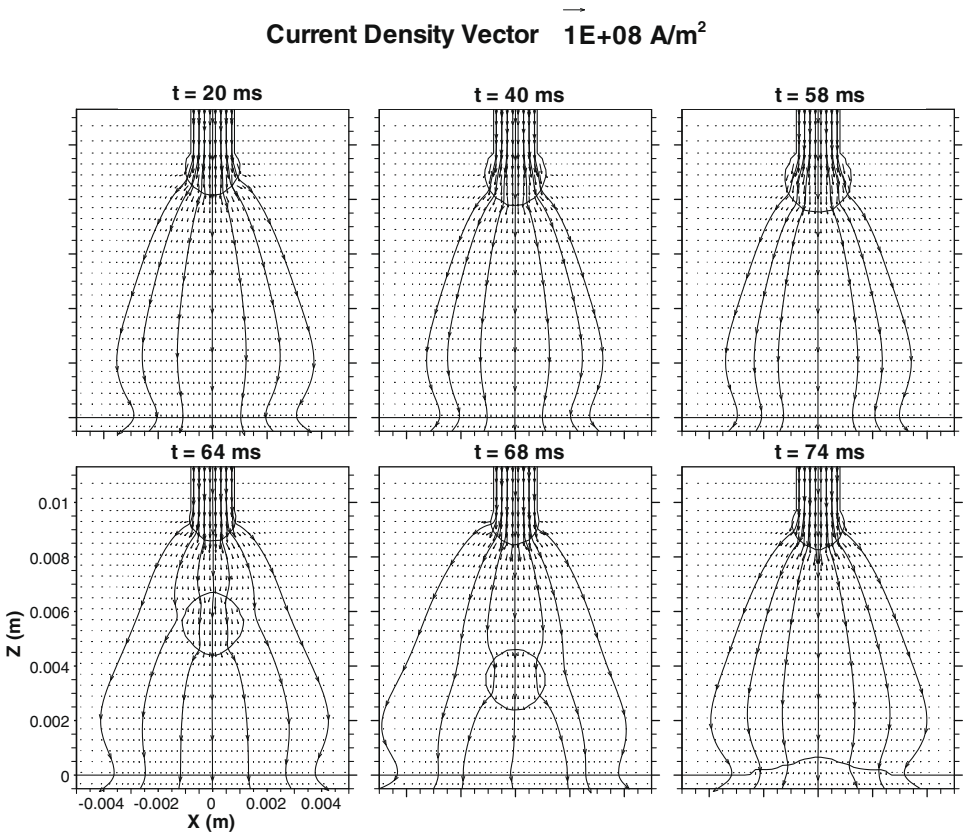

Fig. 4. The corresponding current density distributions as shown in Fig. 2.

with any reasonable shape. The basic procedure for advancing the solution through one time step, Δt, consists of three steps. First, explicit approximations to the momentum Eqs. (2)–(4) are used to find provisional values of the new time velocities at the beginning of the time step. Second, an iterative procedure is used to solve for the advanced time pressure and velocity fields that satisfy Eq. (1) to within a convergence criterion at the new time. Third, the energy equation Eq. (5) is solved.

For the arc plasma domain, a fully implicit formulation is used for the time-dependent terms, and the combined convection/diffusion coefficients are evaluated using an upwind scheme. The SIMPLE algorithm [31] is applied to solve the momentum and continuity equations Eqs. (1)–(5) to obtain the velocity field. At each time step, the current continuity equation Eq. (16) is solved first, based on the updated parameters. The new distributions of current density and electromagnetic force are then calculated for the momentum and energy equations. The momentum equations and the mass continuity equation are then solved in the iteration process to obtain pressure and velocity. The energy equation is solved to get the new temperature distribution. Next, the temperature-dependent parameters are updated, and the program goes back to the first step to calculate the current continuity equation. This process is repeated for each time step until the convergence criteria are satisfied.

The governing differential equations (Eqs. (1)–(5), (16), (20)–(23)) and all related supplemental and boundary conditions are solved through the following iterative scheme:

(1) At $t = 0$, the electrode is set up at an initial position and initial temperature distribution is given to the metal domain. Based on the initial fixed metal domain and temperature distribution, the initial distributions of temperature, velocity, pressure and current are obtained by solving the steady state equations in the arc domain (this procedure is similar to the steps from 5–8 for the steady state).
(2) Surface tension, Marangoni shear stress, electromagnetic force, plasma shear stress and arc pressure are calculated, and other associated boundary conditions are evaluated for the metal domain.
(3) Eqs. (1)–(5) are solved iteratively to obtain pressure, velocity and temperature in the metal domain.
(4) VOF equation Eq. (23) is solved to obtain the new free surface profile for the metal domain. The physical properties in the mesh cells and the boundary conditions within the computing domain are updated.
(5) The current continuity equation Eq. (17) is solved in the whole domain with updated parameters. Current density and the source terms for the magnetic field equations are calculated.
(6) The magnetic filed equations Eqs. (20)–(22) are solved in the whole domain. Electromagnetic forces are calculated for the momentum equations.
(7) Eqs. (1)–(4) and the associated boundary conditions are solved iteratively to get the velocity and pressure distributions of the arc plasma. When solving these equations, the electrode, droplet and the workpiece are treated as fixed inner obstacles.
(8) Energy Eq. (5) is solved in the arc domain to get the new temperature distribution. Thermal physical properties of the arc plasma are updated. From here, the iteration goes back to step 5 to repeat the process for new distribution of current density, velocity, pressure, and temperature, until convergence criteria are satisfied.
(9) Advance to the next time step and back to step 2 until the desired time is reached.

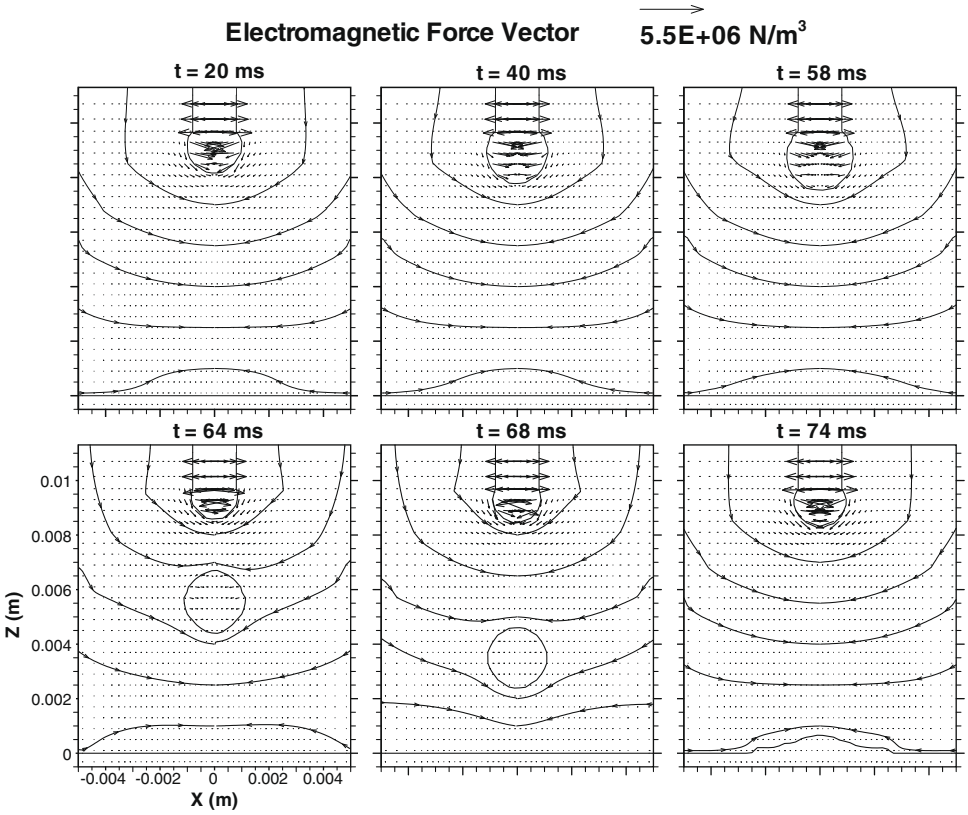

Fig. 5. The corresponding electromagnetic force distributions as shown in Fig. 2.

The above complete transient solution procedures are for the fully coupled model which calculates the plasma arc at each time step. The interaction between the metal zone and plasma zone can be taken into account through the internal boundary conditions. The complete transient solution has been obtained by Hu and Tsai in a 2D model [7]. Although the same procedures are applicable for this 3D model, the computational time becomes prohibitively huge for the 3D case. Therefore, the plasma flow is only updated at a given time interval, and its interaction with the metal flow is either ignored or accounted for by simplified models described in Section 2.

The computational domain for the 3D model is $20 \times 10 \times 17$ mm as shown in Fig. 1. A typical non-uniform mesh has $56 \times 28 \times 70$ cells. The mesh size near the anode axis is set as 0.2 mm. The time step is in the order of 10^{-5} second and is constrained by VOF advection. The computation time for plasma updating at one time step requires 2 hours on latest DELL PCs with a Linux operating system.

4. Results and discussion

A complete 3D mathematical model for the GMAW process is developed, the complete solution for a 3D case can be obtained if the numerical solution procedures proposed by Hu and Tsai [7] are followed. The biggest challenge for such a 3D solution lies in the cost of numerical computation. Normally, the plasma flow can be computed with a relatively large grid size, but the metal flow requires a much smaller grid size in order to resolve various body forces within the tiny droplet. Consequently, the time step restricted by the VOF advection in the metal domain becomes very small. Hu and Tsai used 0.1 mm grid size and 5×10^{-6} s time step in their computations [7]. It is almost impossible to use the same resolutions for the 3D model. For example, in this study, the grid size is 0.2 mm and the average time step is 5×10^{-5} s. The numerical computations showed that the 0.2 mm grid size was not small enough to accurately calculate the balance of the surface tension force and the strong electromagnetic force in the pendant droplet. As it already takes hours to calculate one time step, it is impractical to further reduce grid size. Thus, simplifications must be made based on the interest of current study.

This study focuses on the evolvement of the 3D plasma arc during the metal transfer process in GMAW. Therefore, the fluid flow and heat transfer inside the metal zone can be greatly simplified because they have little effect on the electric and magnetic fields in plasma arc [7]. As plasma arc is greatly affected by the topology of the metal zone and slightly affected by the temperature of the metal zone [1], tracking the topology of the metal zone by VOF method is more important for the model. Thus, the coupling of the plasma arc zone with the metal zone is relaxed by reducing the calculation of the plasma arc from at each time step to at some moments of interest.

In this study, the electrode is a 1.6-mm- diameter mild steel wire and the workpiece is a 5-mm-thick mild steel chunk. The

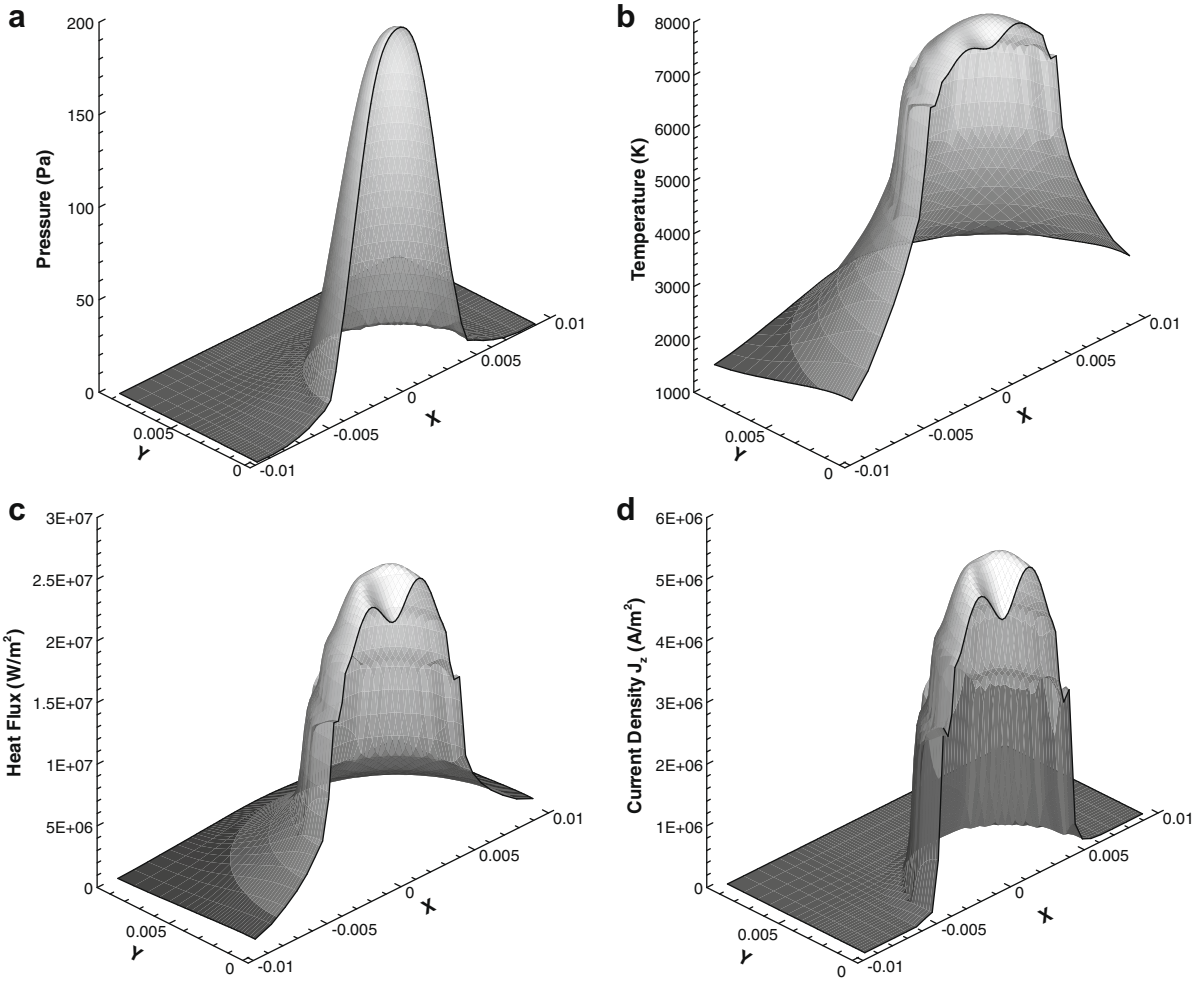

Fig. 6. Distributions at the workpiece surface at $t = 64$ ms: (a) pressure, (b) temperature, (c) heat flux, and (d) current density J_z.

properties of mild steel are taken from [7] in the computation. The shielding gas is argon (Ar). The welding current is 240 A and the equilibrium arc length is 9 mm. The electrode feed rate is set as 4.8 mm/s according to experiments in [32]. The growth of the pendant droplet is controlled by the surface tension force only. This approximation reduces the complexities caused by the strong electromagnetic force, which requires smaller grid size and time step. The droplet is artificially detached from the electrode with the presumed frequency. The period is 60 ms and the temperature of droplet is set as 3000 K according to Hu and Tsai [7–10]. Although this droplet generation mechanism is simplified, reasonable results were obtained. The generated droplet is approximately in a sphere shape similar to that from the experimental observations [32]. The diameter of the generated droplet is determined by the electrode feed rate. The flight of the droplet to the workpiece is subject to the plasma drag force calculated by Eq. (26). This approximation is fairly good because the calculated droplet flight time is 12 ms for a 6 mm distance while the experimental measurement is about 12.5 ms when the initial axial droplet velocity is set as 0.28 m/s according to the experiments [33]. It should be noted if the plasma flow is solved at every time step, then this approximation is not necessary and the drag force can be directly calculated from the plasma flow. The impingement of the droplet onto the workpiece is modeled using the aforementioned governing equations and boundary conditions. However, the effects of arc pressure, plasma drag force, electromagnetic force, and arc heat flux on the workpiece are ignored because the plasma flow is not solved at every time step. This simplification is acceptable because at the moment of impingement, the momentum and energy carried by the droplet is much greater that those from the plasma arc. This simplification is supported by the facts that some droplet impingement models were able to obtain good numerical results even with inaccurate boundary conditions. Hu et al. used 48% for the ratio of the droplet thermal energy to the total input energy transferred to the workpiece [3]. During one droplet impinging period, approximately half of the energy to the weld is abruptly brought in by the droplet during a short moment, while another half is continuously brought in by the arc during the entire period. By raising the droplet temperature to a higher value, in this study, 3000 K, the heat brought in by the arc is partially considered. As this study focuses on the plasma flow instead of the weld pool dynamics, only one droplet impinging onto the workpiece is simulated. Thus, it is fair to ignore the arc heat flux during the impinging process.

Based on the abovementioned approximations, the growth, detachment, and impingement of one droplet in the stationary axisymmetric arc have been computed using this 3D model. Though this case can be done by a 2D model, it is studied first to verify this 3D model. Figs. 2–5 show the plots of the distributions of temperature, electric potential, pressure, velocity, current density, and electromagnetic force on the symmetric plane ($y = 0$) at time $t = 20$, 40, 58, 64, 68, 74 ms, respectively. The famous "bell-shape" plasma arc is observed from the temperature distributions. The highest temperature of the arc column is around 20,000 K and is consistent with the numerical results from the 2D models

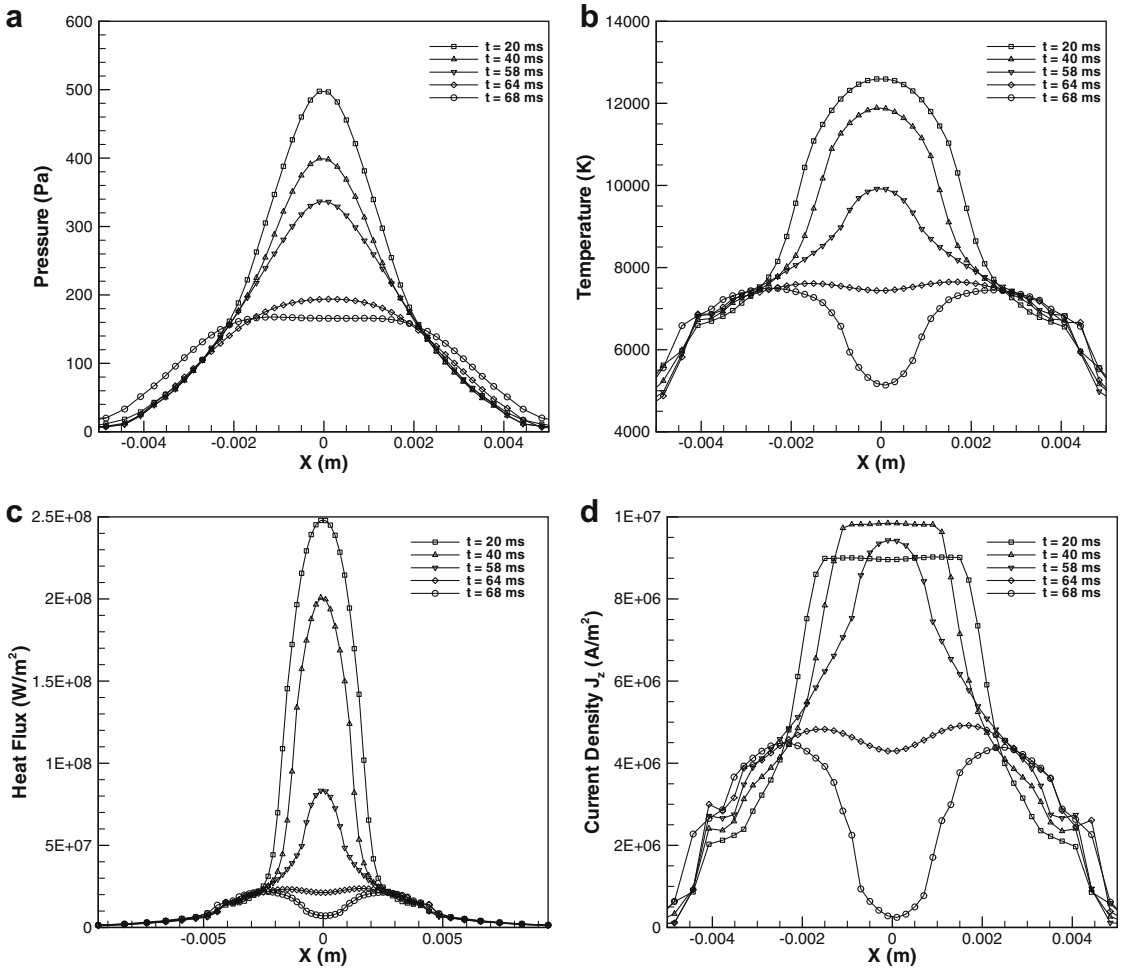

Fig. 7. Evolvement of the distributions at the workpiece surface on the symmetric plane ($y = 0$): (a) pressure, (b) temperature, (c) heat flux, and (d) current density J_z.

[1,7–10] and the experimental measurements for GTAW arcs [34]. Before the detachment, the highest temperate decreases as the droplet grows. It changes from 20,256 K at 20 ms to 19,050 K at 40 ms and then to 18,280 K at 58 ms (2 ms before the detachment). This decrement is resultant from the globular growth of the pendant droplet. As it grows bigger, its surface area becomes larger and consequently the current density diverges more and become smaller. The arc temperature is therefore reduced because the ohmic heating from the current contributes most of the arc energy. The arc temperature boosts up right after the droplet detachment and then falls down as the droplet goes away. The arc between the electrode and the detached droplet is somewhat equivalent to an arc that gradually changes its arc length. Apparently, the shorter arc has a higher arc temperature. The calculated highest arc temperature is 21,742 K at 64 ms, and 20,893 K at 68 ms.

The electric potential varies from 12.5 V at 20 ms to 11.6 V at 40 ms and then to 11.0 V at 58 ms before the droplet detachment. The variation trend is the same as that of the temperate because the electric potential is related to the electric current by $\vec{j} = \sigma_e \nabla \phi$ and the electric conductivity varies little during the temperature range between 18,000 K and 22,000 K. However, after the droplet detachment, the variation trend of the electric potential is different from that of the temperature. It is 13.0 V at 64 ms, increases to 13.2 V at 68 ms, and decreases to 12.4 V at 74 ms. This is because the arc flows around the in-flight droplet. Underneath the in-flight droplet, the electric conductivity of the plasma arc is low at low temperature.

The velocity of the plasma jet also decreases during the droplet growth. The highest axial velocity component drops from 228 m/s at 20 ms to 193 m/s at 40 ms and then to 163 m/s at 58 ms. This again can be accounted for by the variations of the current density. The electromagnetic force caused by the electric current and the self-induced magnetic field is the dominant driving force in the plasma jet. As the current density decreases during the droplet growth, the strength of the pumping force decreases and the plasma jet becomes less strong. The jet velocity may still be low after the droplet detachment if the jet has not fully developed. The highest velocity is only 148 m/s at 64 ms and increases to 226 m/s at 68 ms. The corresponding pressure distributions are shown in Fig. 2(c). The gaps between the pressure contours and the metal

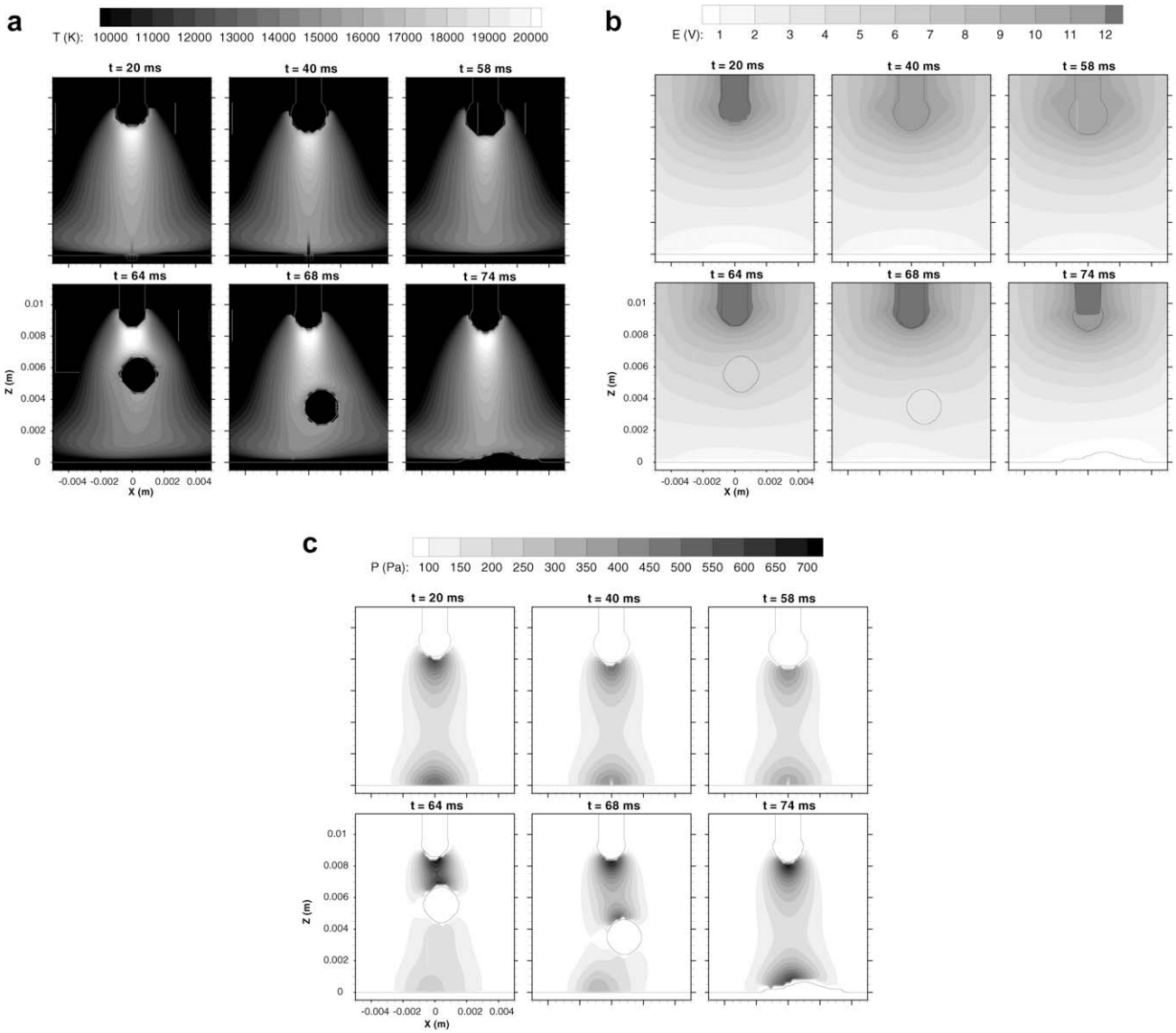

Fig. 8. A typical sequence of temperature, electrical potential, and pressure distributions on the symmetric plane ($y = 0$) for a non-axisymmetric stationary arc: (a) temperature, (b) electrical potential, (c) pressure.

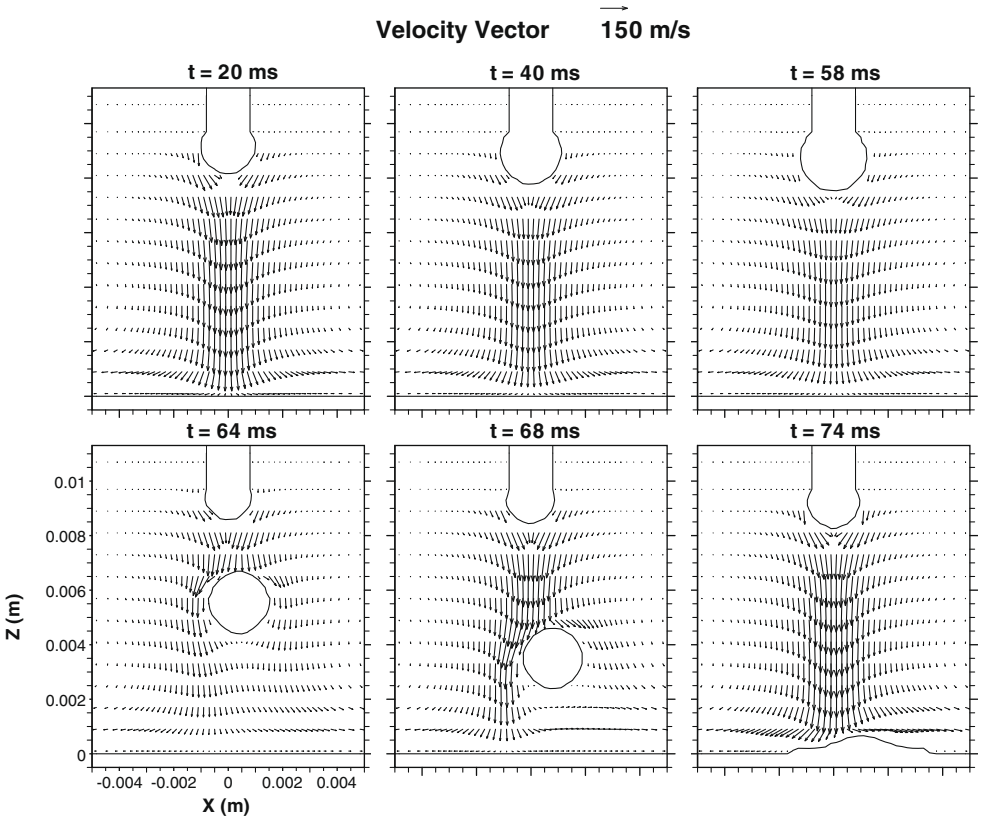

Fig. 9. The corresponding velocity distributions as shown in Fig. 8.

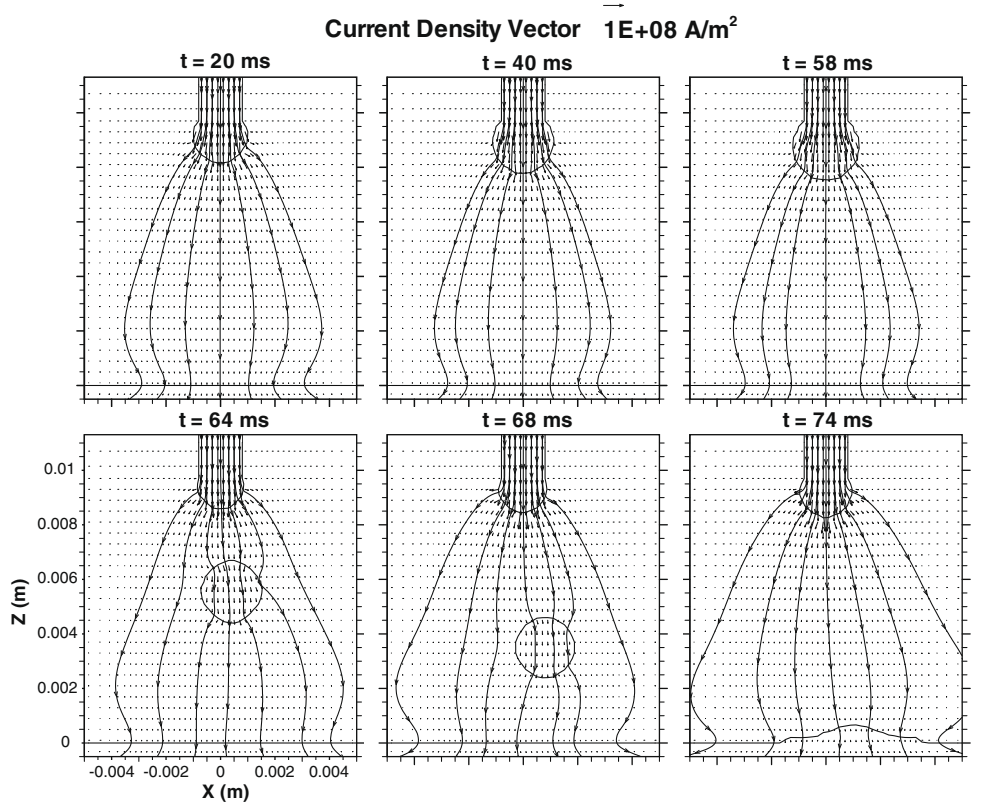

Fig. 10. The corresponding current density distributions as shown in Fig. 8.

zones are due to the relatively large grid size. The high pressures are expected in the arc stagnation regions and their variations are associated with the velocity vector field. The arc pressure is an attaching force to the droplet before the detachment, but once the detachment occurs, it will accelerate the droplet transfer to the workpiece.

The density vector fields are shown in Fig. 4. From the above discussions, it can be seen that the current density distribution is the influential factor in the arc. Arc distributions greatly depend on the topology of the metal zones because the electric conductivity of the metal is much higher than that of the plasma gas. A small change of the electrode shape may cause a great change of the plasma arc. The vectors and streamlines of the electromagnetic force vector are shown in Fig. 5. The streamlines coincide with the isopotential lines because both of them are orthogonal to the electric current. In the plasma zone, the electromagnetic force is the dominant driving force for the plasma jet. In the electrode metal zone, it is a major detaching force on the droplets in GMAW. The balance between the electromagnetic force and the surface tension force mostly determines the droplet size. The modeling of the droplet generation has been studied by some researchers [4,7–10]. A very fine mesh is generally necessary to calculate the strong electromagnetic force.

Fig. 6(a)–(d) show the distributions of pressure, temperature, heat flux, and current density J_z on the workpiece surface at $t = 64$ ms. It can be found that the presence of the droplet alters the distributions greatly as comparing with those in GTAW [35]. The peak of the arc pressure becomes flat, while the distributions of the temperature and current density have a bimodal shape. Actually, these shapes evolve gradually with the growth of the pendant droplet and the descent of the detached droplet. Fig. 7(a)–(d) show the evolvement of these distributions at the workpiece surface and along the symmetric plane ($y = 0$) for pressure, temperature, and current density J_z. These phenomena were studied by Hu and Tsai in their 2D modeling of GMAW [7]. As the pendant droplet grows and falls, the peak of the arc pressure lowers and the shape flattens. The temperature distribution varies in the same trend, but the depression of the peak value is even more and turns out to have a bimodal shape. This is directly related to the bimodal distribution of the electric current when current flows around the droplet. Current does not pass entirely through the droplet to its bottom area (on the contrary to the electrode pendant) due to the higher plasma temperature and the consequent higher plasma electric conductivity in the surrounding area. Fig. 7 also reveals that the temporally invariant Gaussian distributions for the arc pressure, heat flux, and the current density at the workpiece surface cannot reflect the real boundary conditions when modeling the weld pool dynamics in GMAW. However, most weld pool models employed the invariant Gaussian assumptions and obtained good numerical results such as bead shape. The possible explanation is that higher amount of the momentum and energy carried by the droplet to the weld pool.

This 3D model is capable to simulate the droplet transfer in a non-axisymmetric arc. In order to demonstrate the 3D capability, a simple case of moving arc is studied. In this case, the arc moves to the negative x direction at the welding speed of 0.1 m/s. For the purpose of easy implementation, the arc is fixed, while the workpiece and detached droplet move to the positive x direction. It is assumed that the plasma drag force to the droplet in the moving arc is the same as that in the stationary arc, and therefore the droplet has the equal flight time in both cases. Figs. 8–11 shows the same plots for the moving arc as those for the stationary arc in Figs. 2–5. All the plots before the droplet detachment are identical for these two cases because their topologies of the metal zones are identical before the first droplet. The non-axisymmetric effects after the droplet detachment can be clearly seen from these figures. The highest arc temperature is 21,727 K at 64 ms, which is slightly lower than 21,742 K in the axisymmetric case. The difference of the electric potential at this moment is smaller than 0.1 V. The highest axial velocity is 157 m/s when comparing with the previous value of 148 m/s. All these changes can be attributed

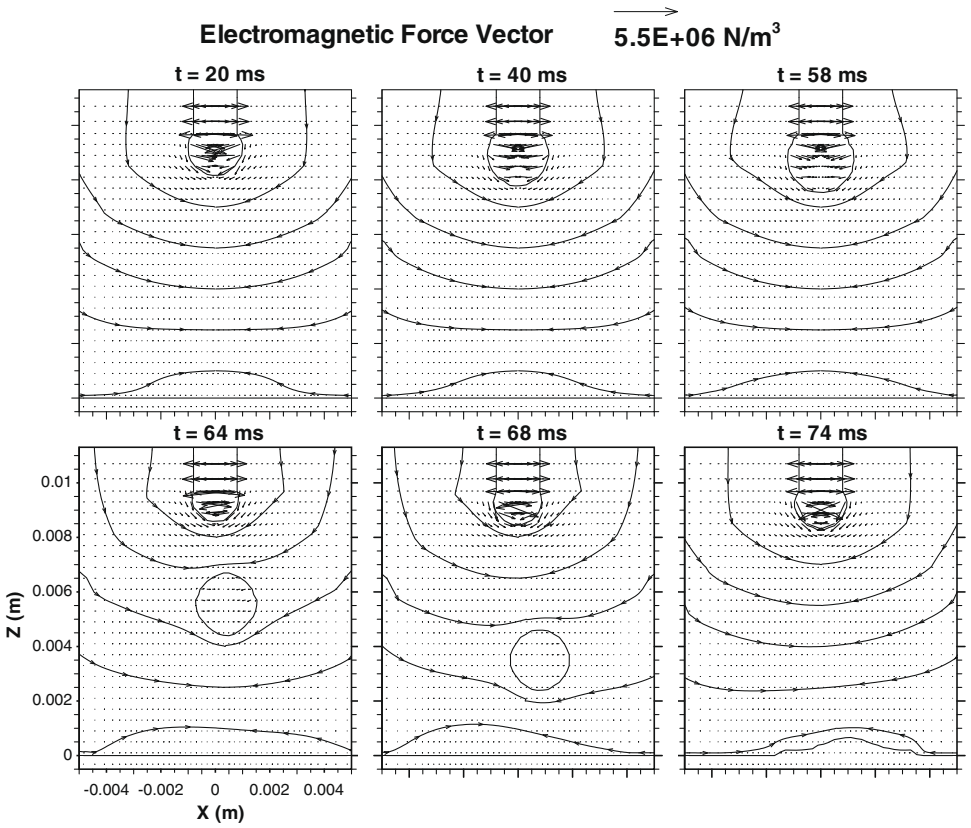

Fig. 11. The corresponding electromagnetic force distributions as shown in Fig. 8.

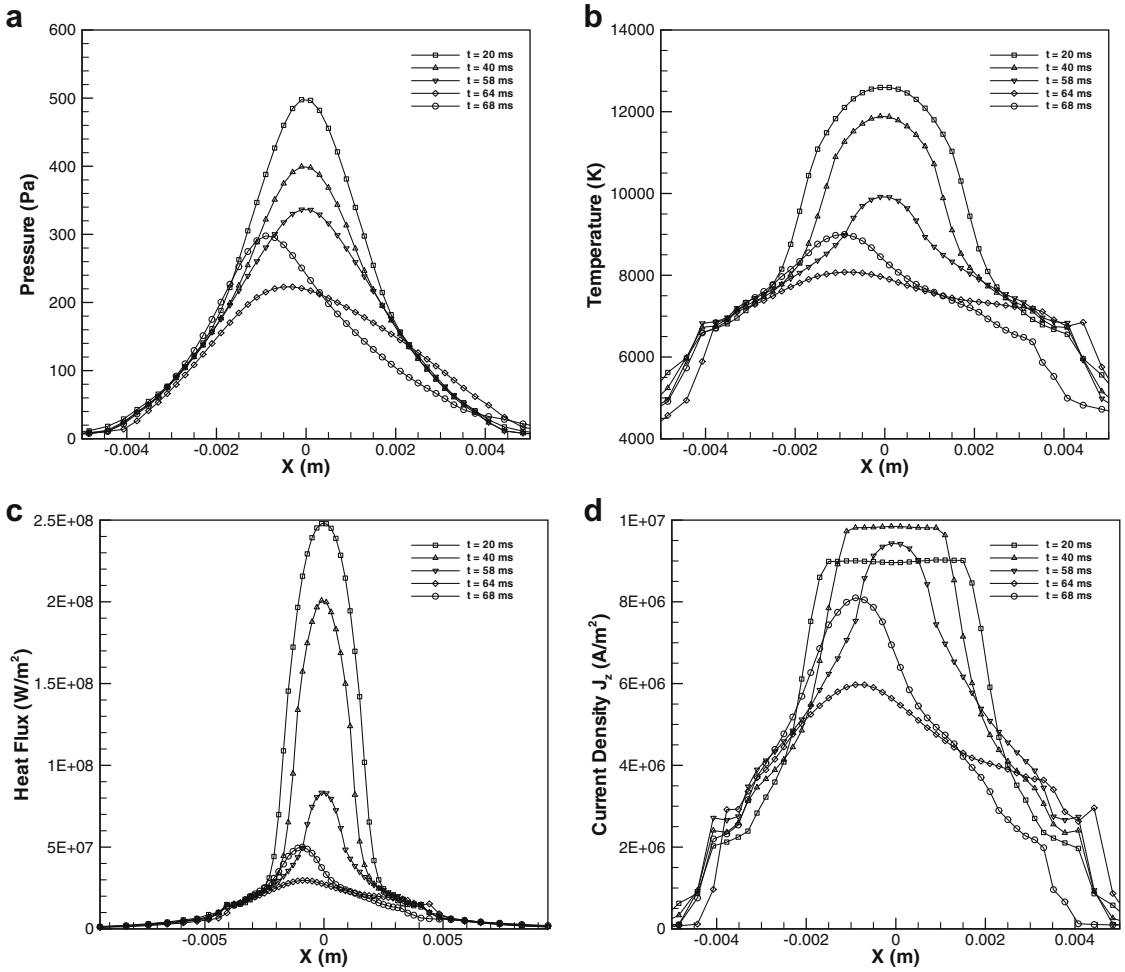

Fig. 12. Evolvement of the distributions at the workpiece surface on the symmetric plane ($y = 0$) for a non-axisymmetric moving arc: (a) pressure, (b) temperature, (c) heat flux, and (d) current density J_z.

to the off-axis droplet which makes the electric current drift from its axisymmetry slightly. The induced electromagnetic force under the pendant droplet also becomes non-axisymmetric, which may propel the droplet to a deflected globular shape observed in many GMAW photographs [28]. This phenomenon is caused by the non-axisymmetric plasma arc, which in turn is caused by the non-axisymmetric topology of the metal zone such as the off-axis droplet and 3D welds or other external perturbations such as external magnetic field [17].

Fig. 12(a)–(d) show the evolvement of the distributions of pressure, temperature, heat flux, and current density J_z in the moving arc. It can be found that these distributions are not axisymmetric again after the droplet detachment. The peaks shift to the arc moving direction gradually as the droplet falls. It is interesting to note that the flat peak of the pressure distribution and the bimodal shape of the temperature and current density distributions disappear. This is because the off-axis droplet cannot perfectly impede the on-axis plasma jet and the jet flow can bring high temperature gas to the bottom area of the droplet.

5. Conclusions

A 3D mathematical model for the metal transfer process in GMAW was formulated in this article. A complete model describing the GMAW welding process is developed, however, the computation of the transient solution of the complete model was prohibitively time-consuming and beyond the capability of the current PCs. In order to study the plasma arc interaction with metal during the metal transfer process, some simplifications have been made. A case of an axisymmetric arc was studied first using this 3D model for the verification purpose. The numerical results agreed well with the previous two-dimensional studies. A case of a moving arc was then computed to demonstrate the 3D capability of the model. The results revealed that the time-invariant Gaussian assumption for the distributions of the arc pressure, heat flux, and current density on the workpiece surface did not represent of the real situation. The calculated distributions for the moving arc were non-axisymmetric and the peaks shifted to the arc moving direction.

References

[1] P.G. Jonsson, T.W. Eagar, J. Szekely, Heat and metal transfer in gas metal arc welding using argon and helium, Metall. Trans. 26B (1995) 383–395.
[2] T. Zacharia, A.H. Eraslan, D.K. Aidun, S.A. David, Three-dimensional transient model for arc welding process, Matall. Trans. 20B (1989) 645–659.
[3] J. Hu, H. Guo, H.L. Tsai, Weld pool dynamics and the formation of ripples in 3D gas metal arc welding, Int. J. Heat Mass Transfer 51 (2008) 2537–2552.
[4] F. Wang, W.K. Hou, S.J. Hu, E. Kannatey-Asibu, W.W. Schultz, P.C. Wang, Modeling and analysis of metal transfer in gas metal arc welding, J. Phys. D Appl. Phys. 36 (2003) 1143–1152.
[5] J. Haidar, A Theoretical Model for Gas Metal Arc Welding, Gas Tungsten Arc Welding. I, J. Appl. Phys. 84 (1998) 3518–3529.
[6] J. Haidar, Predictions of metal droplet formation in gas metal arc welding. II, J. Appl. Phys. 84 (1998) 3530–3540.

[7] J. Hu, H.L. Tsai, Heat and mass transfer in gas metal arc welding Part I: the arc, Int. J. Heat Mass Transfer 50 (2007) 833–846.
[8] J. Hu, H.L. Tsai, Heat and mass transfer in gas metal arc welding. Part II: the metal, Int. J. Heat Mass Transfer 50 (2007) 808–820.
[9] J. Hu, H.L. Tsai, Effects of current on droplet generation and arc plasma in gas metal arc welding, J. Appl. Phys. 100 (2006) 053304.
[10] J. Hu, H.L. Tsai, Metal transfer and arc plasma in gas metal arc welding, ASME J. Heat Transfer 129 (2007) 1025–1035.
[11] H.G. Fan, R. Kovacevic, A unified model of transport phenomena in gas metal arc welding including electrode arc plasma and molten pool, J. Phys. D Appl. Phys. 37 (2004) 2531–2544.
[12] J.F. Lancaster, The Physics of Welding, second ed., Oxford Pergamon, 1986.
[13] G. Xu, W.W. Schultz, E. Kannatey-Asibu, Application of a front tracking method in gas metal arc welding (GMAW) simulation, J. Manufac. Sci. Eng. 127 (2005) 590–597.
[14] P.G. Jonsson, J. Szekely, R.T.C. Choo, T.P. Quinn, Mathematical models of transport phenomena associated with arc-welding processes: a survey, Model. Simul. Mater. Sci. Eng. 2 (1994) 995–1016.
[15] R.T.C. Choo, J. Szekely, R.C. Westhoff, Modeling of high-current arcs with emphasis on free surface phenomena in the weld pool, Welding J. (1990) 346s–361s. Sept.
[16] Y.H. Kang, S.J. Na, A study on the modeling of magnetic arc deflection and dynamic analysis of arc sensor, Welding J. (2002) 8s–13s. Jan.
[17] G. Xu, H.L. Tsai, Three-Dimensional Modeling of Plasma Arc in Arc Welding, Proceedings of IMECE'06, Chicago, USA, 2006.
[18] K.C. Chiang, H.L. Tsai, Shrinkage-induced fluid flow and domain change in two-dimensional alloy solidification, Int. J. Heat Mass Transfer 35 (1992) 1763–1770.
[19] K.C. Chiang, Studies on the Shrinkage-Induced Transport Phenomena during Alloy Solidification, Ph.D. Dissertation, University of Missouri-Rolla, Rolla, MO, 1990.
[20] P.C. Carman, Fluid flow through granular beds, Tans. Inst. Chem. Eng. 15 (1937) 150–166.
[21] K. Kubo, R.D. Pehlke, Mathematical modeling of porosity formation in solidification, Matall. Trans. 16A (1985) 823–829.
[22] G.S. Beavers, E.M. Sparrow, Non-darcy flow through fibrous porous media, J. Appl. Mech. 36 (1969) 711–714.
[23] S.M. Aithal, V.V. Subranmaniam, J. Pagan, R.W. Richardson, Numerical model of a transferred plasma arc, J. Appl. Phys. 84 (1998) 3506–3517.
[24] M.D. Torrey, L.D. Cloutman, R.C. Mjolsness, C.W. Hirt, NASA-VOF2D: A Computer Program for Imcompressible Flows with Free Surfaces, LA-10612-MS, Los Alamos Laboratory, 1985.
[25] J.U. Brackbill, D.B. Kothe, C. Zemach, A continuum method for modeling surface tension, J. Comp. Phys. 100 (1992) 335–354.
[26] H. Schlichting, Boundary-Layer Theory, sixth ed., McGraw-Hill, New York, 1968 (Chap. I).
[27] K.C. Hsu, E. Pfender, Analysis of the cathode region of a free-burning high intensity argon arc, J. Appl. Phys. 54 (1983) 3818–3824.
[28] H.A. Dinulescu, E. Pfender, Analysis of the anode boundary layer of high intensity arcs, J. Appl. Phys. 51 (1980) 3149–3157.
[29] T. Zacharia, S.A. David, J.M. Vitek, Effect of evaporation and temperature-depenedent material properties on weld pool development, Metall. Trans. 22B (1992) 233–241.
[30] D.B. Kothe, R.C. Mjolsness, RIPPLE a new model for incompressible flows with free surface, AIAA J. 30 (1992) 2694–2700.
[31] S.V. Patanka, Numerical Heat Transfer and Fluid Flow, New York, McGraw-Hill, 1980.
[32] L.A. Jones, T.W. Eagar, J.H. Lang, Images of a steel electrode in Ar–2%O_2 shielding during constant current gas metal arc welding, Welding J. 2 (1998) 135s–141s.
[33] L.A. Jones, T.W. Eagar, J.H. Lang, A dynamic model of drops detaching from a gas metal arc welding electrode, J. Phys. D: Appl. Phys. 31 (1998) 107–123.
[34] K.C. Hsu, K. Etemadi, E. Pfender, Study of the free-burning high-intensity argon arc, J. Appl. Phys. 54 (1983) 1293–1301.
[35] J. McKelliget, J. Szekely, Heat transfer and fluid flow in the welding arc, Matall. Trans. 17A (1986) 1139–1148.